Numerical investigation of underground reservoirs in compressed air energy storage systems considering different operating conditions: Influence of thermodynamic performance on the energy balance and round-trip efficiency

Javier Menéndez [a,*], Jesús M. Fernández-Oro [b], Mónica Galdo [b], Laura Álvarez [c], Antonio Bernardo-Sánchez [c]

[a]Sadim Engineering, Oviedo, 33005, Spain
[b]Energy Department, University of Oviedo, Gijón, 33271, Spain
[c]Department of Mining Technology, Topography and Structures, University of León, León, 24071, Spain

[*]Corresponding author: javier.menendez@sadim.es

A B S T R A C T

In the current energy transition, abandoned mines can be used as strategic large scale energy storage systems. Lined mining drifts can store compressed air at high pressure in compressed air energy storage systems. In this paper, three-dimensional CFD numerical models have been conducted to investigate the thermodynamic performance of underground reservoirs in compressed air energy storage systems at operating pressures from 6 to 10 MPa. U-shaped mining drifts with a cross-sectional area of 8 m^2 and a volume of 400 m^3 have been selected as underground reservoir. A 15 cm thick reinforced concrete lining and a 5 m thick rock mass have been considered around the compressed air. Air temperature and pressure variations within the reservoir and heat transfer across the reservoir walls were analyzed for ten compression and expansion cycles considering different operating conditions. Then, the results of the numerical model were used to estimate the preliminary energy balance and the round-trip energy efficiency. To validate the results of the numerical model, a one-dimensional analytical model has been developed. The results obtained show that the power generation and the round-trip energy efficiency increase when the variations in air temperature are reduced. A 4.60% increase in power generation was observed in the expansion process when the air mass flow rate is reduced from 150 to 50 kg s^{-1}. The round-trip efficiency reaches 0.71 for an A-CAES scheme with air mass flow rates of 25 and 50 kg s^{-1} in compression and expansion, respectively. Finally, good agreements have been obtained between analytical and numerical results.

Key-Words: closed mines; A-CAES; energy storage; energy balance; underground reservoir; renewable energies.

Nomenclature

C_v	Specific heat at constant volume (J kg^{-1} K^{-1})
E_C	Energy consumed by the compression train (MWh)
E_T	Energy generated by the expansion train (MWh)
g	Gravity acceleration (m s^{-2})
h	Specific enthalpy (KJ kg^{-1})
$h_{c,in}$	Specific enthalpy of air at inlet of compressor (KJ kg^{-1})
$h_{c,out}$	Specific enthalpy of air at outlet of compressor (KJ kg^{-1})
$h_{t,in}$	Specific enthalpy of air at inlet of turbine (KJ kg^{-1})
$h_{t,out}$	Specific enthalpy of air at outlet of turbine (KJ kg^{-1})
k	Specific heat ratio (-)
L	Tunnel length (m)
$\dot{m}_{in}$	Air mass flow rate in the charge period (kg s^{-1})
$\dot{m}_{out}$	Air mass flow rate in the discharge period (kg s^{-1})
P_a	Air pressure (MPa)
P_c	Air pressure at critical conditions (MPa)
$\dot{Q}$	Surface heat transfer (W m^{-2})
S	Tunnel cross section (m^2)
t	Time (s)
T_1	Temperature on the concrete lining wall (K)
T_2	Temperature on the sandstone rock mass (K)
T_3	External temperature (K)
T_a	Air temperature (K)

T_c	Air temperature at critical conditions (K)
$T_{c,in}$	Air inlet temperature of the compressor (K)
$T_{c,out}$	Air outlet temperature of the compressor (K)
$T^{is}_{c,out}$	Compressor isentropic air outlet temperature (K)
$T^{is}_{t,out}$	Turbine isentropic air outlet temperature (K)
$T_{t,in}$	Air inlet temperature of the turbine (K)
$T_{t,out}$	Air outlet temperature of the turbine (K)
u	Specific internal energy (J kg^{-1})
v	Air velocity (m s^{-1})
V	Storage volume (m^3)
W_c	Compressor input power (MW)
W_t	Turbine output power (MW),
Z	Compressibility factor (-)

Greek symbols

β_i	Compression ratio (-)
η_c	Isentropic efficiency (%)
ρ_a	Air density (kg m^{-3})
π_i	Expansion ratio (-)

Acronyms

A-CAES	Adiabatic compressed air energy storage
D-CAES	Diabatic compressed air energy storage
HES	Hydrogen energy storage
HPC	High pressure compressor
HPT	High pressure turbine
LPC	Low pressure compressor
LPT	Low pressure turbine
LSES	Large scale energy storage
TES	Thermal energy storage
UPSH	Underground pumped storage hydropower
URANS	Unsteady Reynolds-Averaged Navier–Stokes

1 Introduction

Large scale energy storage (LSES) systems are required in the current energy transition to facilitate the penetration of variable renewable energies in the electricity grids [1,2]. The underground space in abandoned mines can be a solution to increase the energy storage capacity with low environmental impacts [3-5]. Therefore, underground pumped storage hydropower (UPSH), compressed air energy storage (CAES) and hydrogen energy storage (HES) systems can be installed using the abandoned mining drifts as subsurface reservoirs. Recent research works analyzed the feasibility of using abandoned mines as subsurface reservoirs of UPSH plants [6-9]. Currently, two diabatic CAES (D-CAES) plants are under operation in the world using rock salt formations as compressed air reservoir [10-12]. However, there are no commercial CAES plants in abandoned mines or tunnels. Temperature and pressure variations are produced within the underground reservoirs during the operation of CAES systems. Therefore, the thermodynamic response is essential to properly design the underground reservoir of A-CAES systems to ensure the stability and optimize the energy balance. Constant heat transfer coefficient are normally employed in analytical models to determinate the behavior of the underground reservoir during the charging and discharging processes [13-14]. Experimental studies of adiabatic CAES (A-CAES) systems have been carried out in lined tunnels to analyze the thermo-mechanical performance using different operating conditions and sealing layers [15,18]. Schmidt et al. [19] conducted a geomechanical modelling to investigate the effects of cyclic loading in the underground reservoir of CAES systems considering a pressure range from 4.5 to 7.5 MPa. Moderate deformations were observed during the simulations for lined and unlined tunnels. Alvarez et al. [20] developed analytical and numerical studies to analyze the thermodynamic performance of CAES reservoirs in closed mines considering a 35 cm thick concrete lining and fiber-reinforced plastic and steel as sealing layers. They analyzed the thermal energy balance across the sealing layer and the temperature fluctuation in the concrete lining and sandstone rock mass and concluded that no temperature fluctuations were obtained in the rock mass. Kushnir et al. [21] studied

the temperature and pressure fluctuations within storage caverns in rock formations. They concluded that, compared to adiabatic reservoirs, the heat flux across the reservoir walls imply air temperature and pressure variations within the reservoir. Sarmast et al. [22] analyzed the performance of small scale CAES systems using cased well to store thermal and mechanical energy. The coupled thermo-mechanical performance has been studied in lined rock salt formations subjected to cyclic loading to evaluate the stability and serviceability of the caverns [23,24]. Mohanto et al. [25] conducted a numerical study to investigate the thermo-mechanical response of a horizontal wellbore as underground cavern of a CAES plant. They concluded that large deformation are generated in the rock mass during the operation of CAES plants. A pilot cavern excavated at shadow depth in Korea for CAES systems was used to investigate the excavation damage zone in lined rock caverns [26,27]. They concluded that the tensile fractures and the air leakage could be reduced if the excavation damage zone is minimized. Chen et al. [28] carried out a thermal analysis of gas storage in rock salt formation during gas injection and production. The performance of A-CAES systems with integrated packed bed thermal energy storage was investigated by Tola el al. [29]. They considered a 100 MW CAES plant and concluded that, depending on the turbine operation mode, round-trip energy efficiencies between 0.71-0.77 can be achieved. Other research works on performance, techno-economical and dynamic modelling of A-CAES systems with thermal energy storage systems have also been carried out [30-34]. He et al. [35] developed a study to estimate the required cavern volume for different heat transfer conditions and operating modes. Adiabatic wall conditions, isothermal, and convective heat transfer were considered for the current cavern at the Huntorf CAES plant. They concluded that reduced temperature fluctuations lead to increase the mass storage within the cavern. An analysis of the potential underground storage capacity using CAES systems in India and the UK was carried out [36, 37]. Xu et al. [38] developed a 3D thermo-mechanical analysis of an underground compressed air energy storage. The analyzed two different plugging schemes in abandoned mining drifts. Mousavi et al. [39] conducted a thermodynamic modeling and economic analysis of an A-CAES system based on cascade packed bed thermal energy storage. To reduce greenhouse gas emissions, an innovative cogeneration system composed of CAES, organic Rankine cycle, and CO_2 capture units was proposed by Zeynalian et al. [40]. An exergoeconomic analysis was carried out by Razmi and Janbaz [41] for a cogeneration system composed of CAES, organic Rankine cycle, and absorption-compression refrigeration cycle. A hybrid energy production/storage system comprising a CAES system, a heliostat-driven Brayton cycle, and a hydrogen production unit was proposed by Alirahmi et al [42]. CAES systems can also be combined with renewable energies such as wind and biomass gasification [43,44]. Although some authors consider circular caverns to store the compressed air [17, 20], U-shaped tunnels are considered in this work, which require a lower volume of reinforced concrete to reach the same volume of compressed air within the reservoir.

In this paper, a disused u-shaped mining drift in an abandoned mine with a constant volume of 400 m^3 has been selected as underground reservoir of CAES systems. A 15 cm thick concrete lining and a 5 m thick rock mass have been employed in the model around the compressed air. Three-dimensional CFD numerical models were developed to investigate the thermodynamic response of the compressed air inside the proposed reservoirs for ten compression and expansion cycles considering different operating conditions at air pressures from 6 to 10 MPa. The air temperature, pressure and density variations within the reservoir and the heat transfer across the reservoir walls have been analyzed in all scenarios. Moreover, the heat transfer coefficient on the reservoir walls was also estimated during the simulations. Finally, a CAES scheme is proposed to evaluate the preliminary energy balance and the round-trip efficiency. Two compression and expansion stages with integrated thermal energy storage system were considered to evaluate the power consumption and generation. The charging and discharging times obtained in the numerical study were used to estimate the power consumption and generation and the round-trip energy efficiency.

2 Materials and methods

2.1 Problem statement

An underground reservoir located in an abandoned mine has been considered to simulate the thermodynamic response and the preliminary energy balance considering different operating conditions in the compression and expansion processes. The cross-sectional area of the reservoir is shown in Fig. 1. A disused u-shaped mining drift with a cross-sectional area of 8 m^2 (3x3 m) and a volume of 400 m^3 is

used to store compressed air at operating pressures from 6 to 10 MPa. A 15 cm thick reinforced concrete lining and a 5 m thick rock mass has been considered around the air. An air inlet temperature in the underground reservoir of 310 K is considered during the compression process. Air temperature and pressure variations within the underground reservoir, heat flux through the reservoir walls and the charging and discharging times have been analyzed considering air mass flow rates of 25 and 100 kg s^{-1} in the compression process and 50 and 150 kg s^{-1} in the expansion process. Ten cycles of compression and expansion have been simulated considering storage stages of 50 s between charging and discharging. The results obtained in the numerical simulations were used to estimate the preliminary energy balance and the round-trip efficiency of the CAES system. A CAES plant scheme with two compression and expansion stages and a thermal energy storage system is proposed to analyze the energy balance.

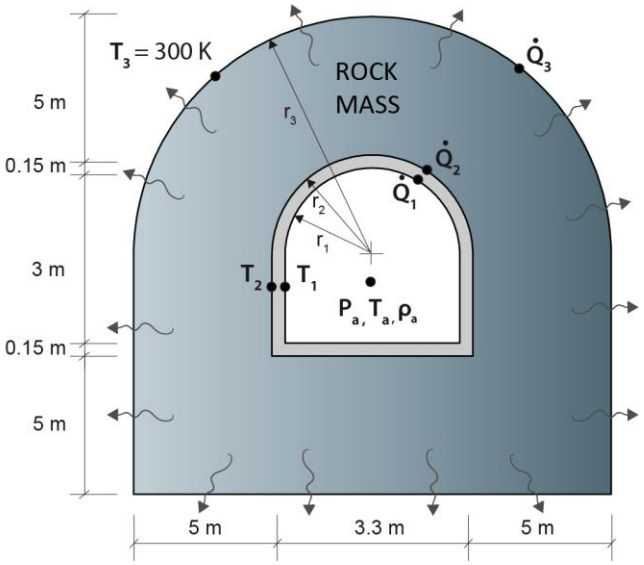

Fig. 1. Cross-sectional area of the underground reservoir with a 15 cm thick reinforced concrete lining.

2.2 Mathematical modelling

A one-dimensional mathematical model has been developed in MATLAB to analyze the thermodynamic response of the underground reservoir considering different operating conditions. Assuming a constant volume of the underground reservoir and based on the mass and energy conservation principles, Kushnir et al. [21,45] applied the following Eqs. (1)-(3) to analyze the thermodynamic response of the compressed air inside the underground reservoir. The compressibility factor can be estimated by applying Eq. (4), adopting the Berthelot gas state equation [2]. However, the compressibility factor of the air in the temperature and pressure fields considered differs insignificantly from the unit (0.3-0.5%) and does not influence the simulation result.

$$V\frac{d\rho}{dt} = \dot{m}_{in} - \dot{m}_{out} \tag{1}$$

$$V\rho C_v \frac{dT}{dt} = \dot{m}_{in}\left(h_i - h + ZRT - \rho\left(\frac{\partial u}{\partial \rho}\right)_T\right) - \dot{m}_{out}\left(ZRT - \rho\left(\frac{\partial u}{\partial \rho}\right)_T\right) - \dot{Q} \tag{2}$$

$$p = Z\rho RT \tag{3}$$

$$Z = 1 - \frac{9p}{128\,p_c}\frac{T_c}{T}\left(\frac{6T_c^2}{T^2} - 1\right) \tag{4}$$

where V is the storage volume (m^3), p, ρ and T represent the air pressure (Pa), density (kg m^{-3}) and temperature (K) within the underground reservoir, respectively. $\dot{m}_{in}$ and $\dot{m}_{out}$ are the air mass flow rate in compression and expansion, (kg s^{-1}). C_v is the constant volume specific heat (J kg^{-1} K^{-1}), u and h denote the specific internal energy (J kg^{-1}) and specific enthalpy (J kg^{-1}). $\dot{Q}$ represents the heat flux across the reservoir walls (J s^{-1}), Z is the compressibility factor and R is the gas constant. T_c and p_c represent the critical temperature and pressure values of the air.

2.3 CFD Numerical modelling

The CFD software Fluent 17.0 was used to simulate the compression and expansion processes that occur in the underground reservoir. This code was employed to solve the 3-D Unsteady Reynolds-Averaged Navier–Stokes (URANS) equations for compressible flow. SIMPLE algorithm was used to solve the pressure-velocity coupling for the iterative process. The energy conservation equation and the RNG k-ε turbulence model were also selected. A three-dimensional numerical model of a u-shaped mining drift has been created using Gambit software. The computational domain is 50 m in length and includes both the fluid area and the solid areas around the fluid. The configuration of the simulated model is shown in Fig. 2. The external part of the model corresponds to the sandstone outside the mine. The reservoir is reinforced with a 15 cm thick concrete lining and is finished with a dead-end. The entire geometry is meshed with 2,404,572 number of hexahedral and tetrahedral elements. Finer mesh is defined in the concrete zone and the air zone, the grids have a higher density in these regions, where the gradients of the flow characteristics are extremely important. The quality of the grid was measured using skewness and element quality indicators. A maximum skewness of 0.62 (less than 0.7) and an average element quality of 0.82 were obtained.

Two models with different air mass flow rates of air charging and discharging have been simulated. Three different types of material (air, concrete and rock mass) are used to simulate the heat transfer process between the pressurized air inside the underground reservoir and the surrounding media. The air is defined as ideal-gas to allow simulation of the compression process. The heat transfer is produced by convection between the compressed air and the concrete lining and by conduction between concrete lining and rock mass. To simulate the concrete layer existing between the air and the rock mass, a solid material zone is defined. The rock mass zone is also defined as solid material. In addition, a series of thermal properties are imposed on the rock mass and the concrete zone to simulate conduction heat transmission. The air mass flow rate was selected as boundary condition at the inlet of the mining drift. An inlet temperature in the reservoir of 310 K and a temperature of 300 K at the end of the model (rock mass) were also considered as boundary conditions. The rock mass temperature increases with the increase of mining depth [46]. The rock mass temperature is well known after many decades of coal mining activity. The summary of the boundary conditions is presented in Table 1. The rock mass temperature is well known after many decades of mining activity. To ensure the solution convergence, a time step of 0.01 s and second order discretization schemes were set. The residual values for convergence were fixed at 10^{-4} for all equations.

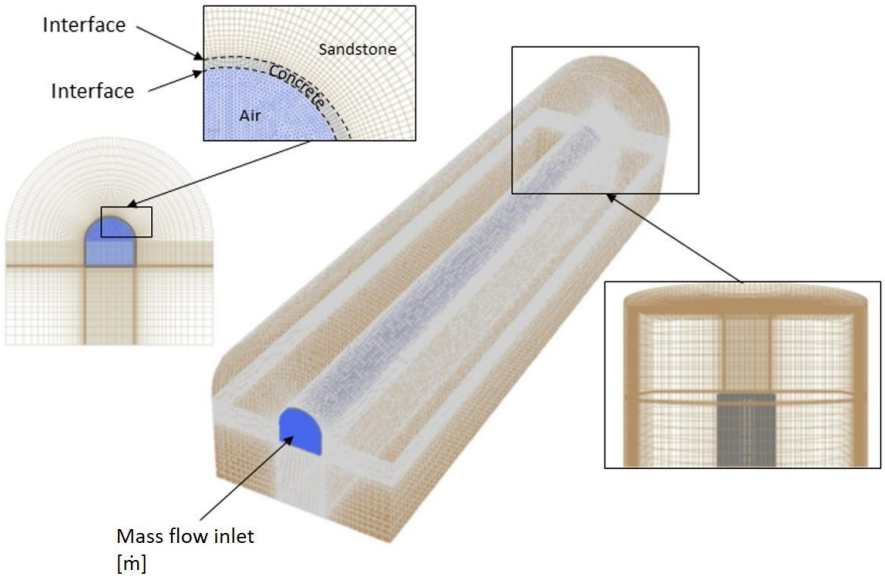

Fig. 2. Model grid and boundary conditions.

Table 1
Boundary conditions

Boundary conditions	Model 1	Model 2
Charge - air mass flow rate (kg s^{-1})	100	25
Discharge – air mass flow rate (kg s^{-1})	150	50
Air inlet temperature (K)	310	300
Rock mass temperature (K)	300	300

2.4 Material properties

The material properties used in the numerical model are indicated in Table 2. Specific heat, thermal conductivity, volume and density of air, reinforced concrete and rock mass properties have been considered in the simulations to determinate the thermodynamic performance during the charging and discharging of the underground reservoir. A thermal conductivity of 1.6 W $m^{-1}K^{-1}$ has been considered for the reinforced concrete. Note that the thermal conductivity of the concrete lining could be increased by adding natural flake graphite to the ordinary Portland cement [47,48].

Table 2
Material properties [17, 20]

Material	Specific heat (J kg^{-1} K^{-1})	Thermal conductivity (W m^{-1} K^{-1})	Volume (m^3)	Density (kg m^{-3})
Air	1,006	0.0242	400	1.17
Concrete	1,000	1.60	75	2,500
Rock mass	711	5.00	7,143	2,600

2.5 Grid independence test

A grid independence analysis has been carried out to improve the accuracy of the numerical simulation results. Four grid sizes were selected for a grid independent study. The thermal energy balance across the reservoir walls was compared for ten cycles using air mass flow rates of 100 kg s^{-1} and 150 kg s^{-1} in compression and expansion, respectively. The results of the grid independence test are presented in Table 3. According to the results obtained, a mesh model with 2,404,575 grids was chosen to optimize the computing efficiency and cost.

Table 3
Grid independence analysis.

Grids (x10^6)	Thermal energy balance (kWh)	Error (%)	Computational time (h)
1.58	289.45	7.97	355.56
2,01	301.40	4.17	456.67
2.40	313.12	0.44	588.89
3.17	314.51	-	744.44

2.6 Preliminary energy balance

The simplified scheme of the A-CAES system considered in this study is presented in Fig. 3. The compression train includes a low pressure compressor (LPC) and a high pressure compressor (HPC). Between the LPC and the HPC, an intercooler heat exchanger is employed to reduce the air temperature and therefore the energy consumption in the HPC. The HPC is followed by a thermal energy storage (TES) system, where the thermal energy generated in the HPC is recovered. A system based on packed bed thermal energy storage has been selected. Then, the pressurized air is stored in the underground reservoir at operating pressure (6-10 MPa). The expansion train includes a high pressure turbine (HPT) and a low pressure turbine (LPT). During the discharge process, the compressed air is heated in the TES and expanded in the HPT and LPT to generate electricity. Compressors and turbines operate at a fixed point in nominal operating conditions. The throttling valve between the TES and the HPT reduces the pressure to the operating values at the HPT (6 MPa), therefore kept constant for the entire duration of the discharge phase.

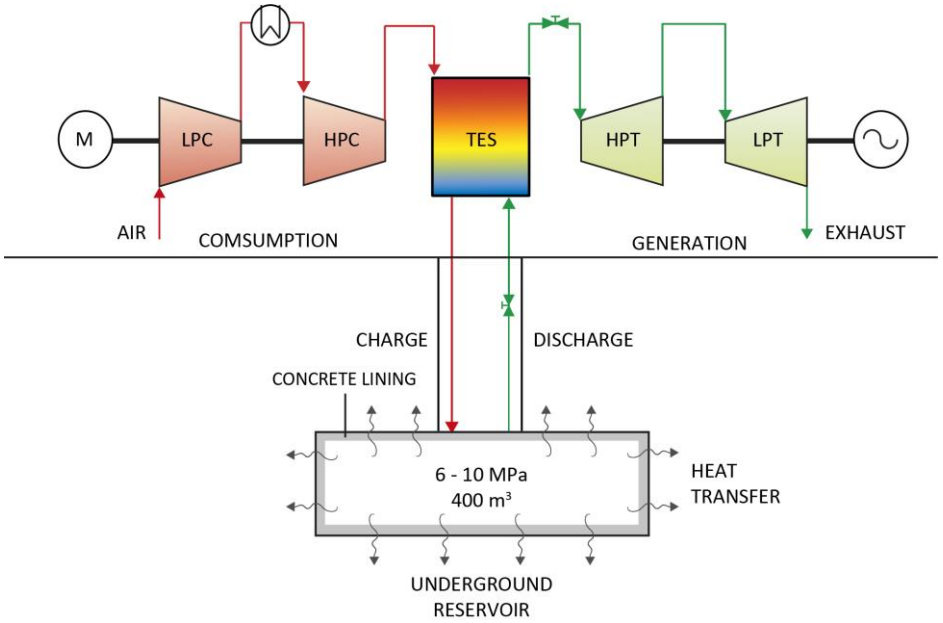

Fig. 3. Simplified scheme of the A-CAES using an abandoned mine as underground reservoir and considering two stages of compression and expansion.

The preliminary energy balance of the CAES system has been analyzed considering the charging and discharging times obtained in the numerical simulations. The energy consumption and production can be determined by multiplying the power of the compressors and turbines by the charging and discharging time, respectively. The input power of LPC and HPC has been estimated by an energy balance neglecting changes in kinetic energy [30,49]. Isentropic air outlet temperature is calculated using the compression ratio as $\beta_i = p_{out}/p_{in}$ and specific heat ratio, k, by applying Eq. (5). The specific heat ratio is defined as the ratio between the specific heats at constant pressure and volume. Air outlet temperature at each compressor was computed using compressor isentropic efficiency as indicated in Eq. (6). Finally, the input power of the compressors is obtained by applying Eq. (7).

$$T_{c,out}^{is} = T_{c,in}(\beta_i)^{\frac{k-1}{n}} \quad (5)$$

$$\eta_c = \frac{T_{c,out}^{is} - T_{c,in}}{T_{c,out} - T_{c,in}} \quad (6)$$

$$W_c = \dot{m}_c\left(h_{c,out} - h_{c,in}\right) \quad (7)$$

where, $T^{is}_{c,out}$ is the compressor isentropic air outlet temperature (K), $T_{c,in}$ is the air inlet temperature of the compressor (K), β_i=$\beta_{HPC,}$ β_{LPC} is the compression ratio, η_c is the isentropic efficiency, $T_{c,\,out}$ is the outlet temperature at each stage (K), W_c is the compressor input power (MW), $\dot{m}_c$ is the air mass flow rate in the compression stage (kg s^{-1}) and $h_{c,out}$ and $h_{c,in}$ are the specific enthalpy of air at the outlet and inlet of the compressor, respectively (KJ kg^{-1}).

Using the approach adopted for the LPC and HPC, the HPT and LPT were modelled through similar considerations for mass and energy balances. The isentropic air outlet temperature of the turbines is obtained using the expansion ratio *(π_i=p_{in}/p_{out})* and turbine isentropic efficiency by applying Eq. (8) and Eq. (9). The output power of the HPT and LPT is calculated by applying Eq. (10).

$$T_{t,out}^{is} = T_{t,in}/(\pi_i)^{\frac{k-1}{k}} \quad (8)$$

$$\eta_t = \frac{T_{t,in} - T_{t,out}}{T_{t,in} - T_{t,out}^{is}} \quad (9)$$

$$W_t = \dot{m}_t\left(h_{t,out} - h_{t,in}\right) \quad (10)$$

where, $T^{is}_{t,out}$ is the turbine isentropic air outlet temperature (K), $T_{t,in}$ is the inlet temperature of the turbine (K), π_i=$\pi_{HPT,}$ π_{LPT} is the expansion ratio, η_t is the turbine isentropic efficiency, $T_{t,out}$ is the outlet temperature at each stage (K), W_t is the turbine output power (MW), $\dot{m}_t$ is the air mass flow rate in each expansion stage (kg s^{-1}) and $h_{t,out}$ and $h_{t,in}$ are the specific enthalpy of air at the outlet and inlet of turbine, respectively (KJ kg^{-1}). Finally, the round-trip energy efficiency of the CAES system can be easily calculated by applying Eq. (11) as the ratio of the electrical energy generated by the expansion train (E_T) and the electricity consumed by the compression train (E_C).

$$\eta_{CAES} = \frac{E_T}{E_C} \quad (11)$$

3 Results and discussion

3.1 Numerical model results

Two different CAES systems with air mass flow rates of 25 and 100 kg s^{-1} in compression and 50 and 150 kg s^{-1} in the expansion process have been analyzed for ten operating cycles considering air pressures from 6 to 10 MPa. Air pressure evolution, temperature and density are shown in Fig. 4 for the indicated air mass flow rates. Air pressure shows a trend similar to temperature and density, and slight variations are observed during the storage stages. In the first cycle, the air pressure varies from atmospheric pressure to the maximum operating pressure. Air temperature rises sharply in the first cycle due to the high air mass flow rates. The air compression process is very fast while the heat transfer process through the reservoir walls is slower, so a quasi-adiabatic process occurs at the beginning of the compression stage. As observed in the trends of air temperature and heat transfer across the reservoir walls, when the heat transfer increases, the air temperature begins to decrease. Air temperature increases when the air mass flow rate increases, reaching 322 K in the fifth cycle for 25-50 kg s^{-1} (Fig. 4c) and 335 K for 100-150 kg s^{-1} (Fig. 4d) after air charging. At the beginning of the air charging (first cycle) the air temperature is not

stable due to the convective effects existing in the 3D model. The air temperature decreases in both models during the storage stages after air charging and increase after air discharging. Air density within the underground reservoir decreases when the air mass flow rate increases. Considering the same volume for both models, the results obtained indicate that the storage capacity increases when the air temperature inside the reservoir decreases and the air density increases.

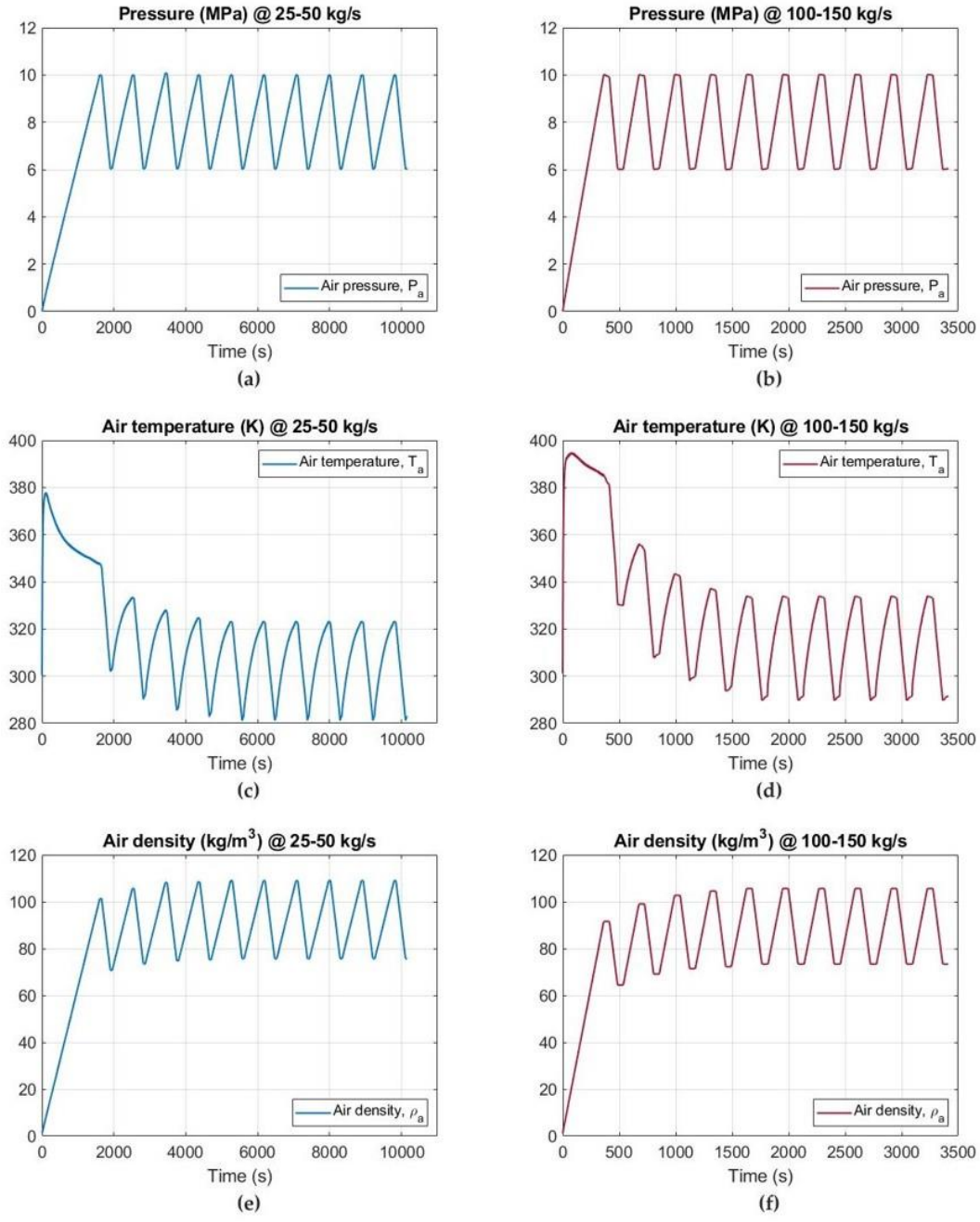

Fig. 4. Air pressure, temperature and density for ten cycles of compression and expansion considering different air mass flow rates. (a) Air pressure @25-50 kg s^{-1}; (b) Air pressure @100-150 kg s^{-1}; (c) Air temperature @25-50 kg s^{-1}; (d) Air temperature @100-150; (e) Air density @ 25-50 kg s^{-1}; (f) Air density @100-150 kg s^{-1}.

Fig. 5 depicts the surface heat flux across the surface between the compressed air and concrete lining (Q_1) and the wall temperature (T_1). The surface heat transfer exhibits a trend similar to wall temperature in both models. During the storage stages, the surface heat flux and the wall temperature decrease after air charging and increase after air discharging. Thermal energy can be transferred or captured by the system depending on the direction of the heat flux as shown in Fig. 5a and Fig. 5b. The thermal energy balance transferred to the surrounding media across the reservoir walls after ten cycles of air charging and

discharging reaches 658 and 626 kWh for air mass flow rates of 25-50 and 100-150 kg s^{-1}, respectively. The compressed air has a higher temperature than concrete lining after air charging and therefore the compressed air is cooled at this stage. Conversely, the concrete lining temperature is higher after air expansion so the compressed air is heated. The wall temperature reaches 316 and 325 K after air charging considering air mass flow rates of 25 and 100 kg s^{-1}, respectively. Negligible temperature variations of 0.3 K were observed on the surface between the concrete lining and rock mass (T_2). In general, no temperature fluctuations are produced on the rock mass around the concrete lining, remaining a constant temperature of 300 K throughout the process that has been investigated.

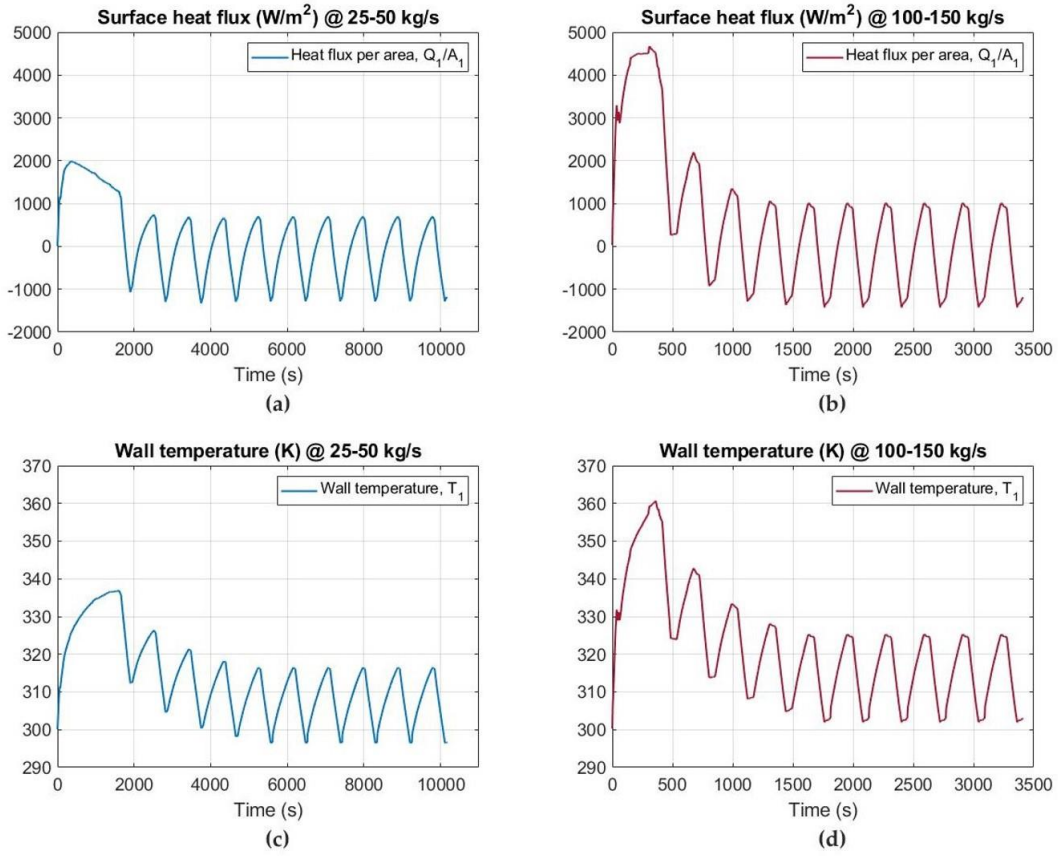

Fig. 5. Surface heat flux across the reservoir walls and wall temperature for ten compression and expansion cycles considering different air mass flow rates. (a) Surface heat flux @25-50 kg s^{-1}; (b) Surface heat flux @100-150 kg s^{-1}; (c) Wall temperature @25-50 kg s^{-1}; (d) Wall temperature @100-150 kg s^{-1}.

A comparative analysis of heat transfer coefficient, wall temperature, heat transfer and air temperature is presented in Fig. 6 considering air mass flow rates of 25 and 100 kg s^{-1} for the first operating cycle from 0.1 to 10 MPa. In the first cycle, the air pressure varies from atmospheric pressure to 10 MPa. Although the heat transfer coefficient is normally considered constant in similar research works, the results obtained in the simulations show that it depends on the operating conditions and varies throughout the air charging process. The heat transfer coefficient reaches 61 W m^{-2} K^{-1} after air charging considering an air mass flow rate of 100 kg s^{-1} and is reduced down to 26 W m^{-2} K^{-1} for 25 kg s^{-1} (Fig. 6a). The concrete wall temperature and the surface heat flux across the concrete wall are shown in Fig. 6b and Fig. 6c, respectively. The evolution of the air temperature within the reservoir is presented in Fig. 6d, increasing significantly when the air mass flow rate increase up to 100 kg s^{-1}. Small fluctuations are observed in the first cycle due to convective effects in the 3D CFD model. The red curves represent the model with higher air mass flow rates (100 kg s^{-s}), where the convective effects are more pronounced and produce greater fluctuations during the first operation cycle. However, the fluctuations disappear when the number of operating cycles increases and the model is stabilized. As indicated in Fig. 6c, the thermal energy transferred to the surrounding media across the reservoir walls after the first cycle reaches 396 kWh for the CAES systems with an air mass flow rate of 25 kg s^{-1} and 216 kWh for 100 kg s^{-1}. The thermal energy is higher in the model with a lower air mass flow rate due to the long air charging time. Fig. 7 shows the

detail of the air temperature within the lined mining drift and the concrete temperature around the compressed air. Air and concrete temperatures are higher at the roof of the mining drifts. As indicated previously, the air temperature decreases at the end of the expansion process and the concrete lining has a higher temperature at this stage (Fig. 7a). Therefore, the surrounding media transfers thermal energy to the system. Conversely, the air temperature is higher than the temperature of concrete lining and rock mass during the compression process (Fig. 7b).

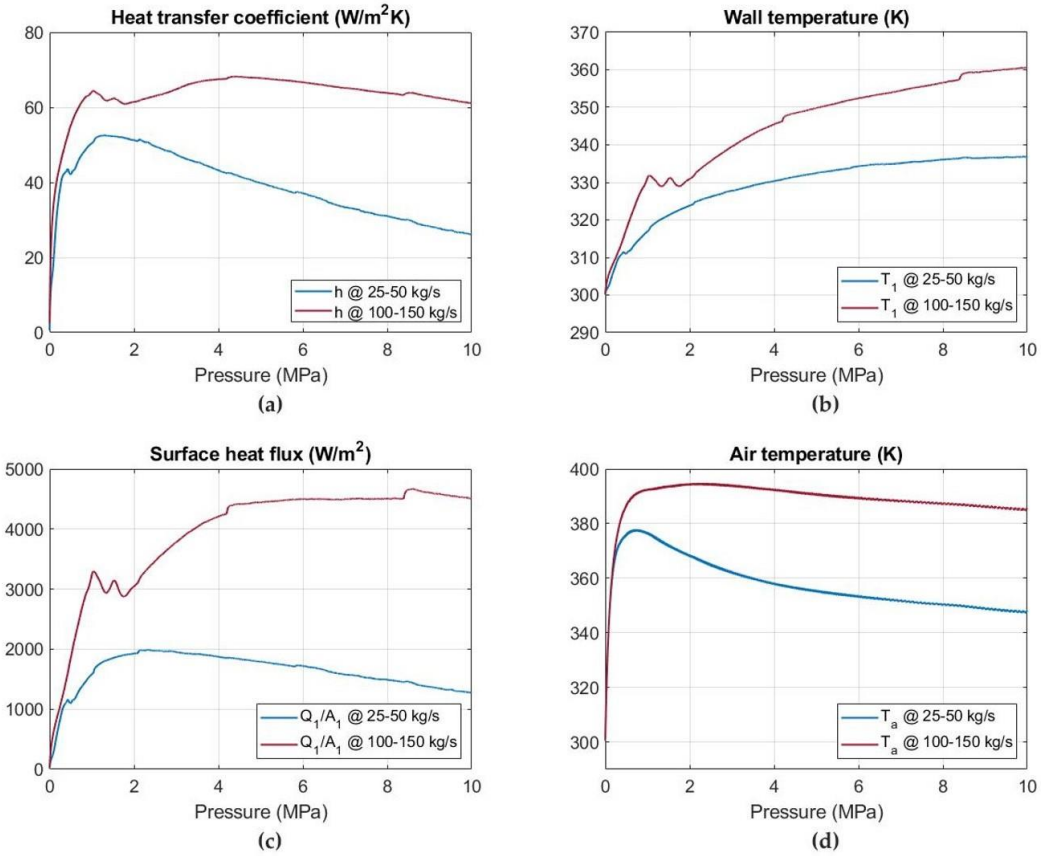

Fig. 6. Comparative analysis between air mass flow rates of 25-50 kg s^{-1} and 100-150 kg s^{-1} for the first operating cycle from 0.1 MPa to the maximum pressure of 10 MPa. (a) Heat transfer coefficient; (b) Wall temperature; (c) Surface heat flux; (d) Air temperature.

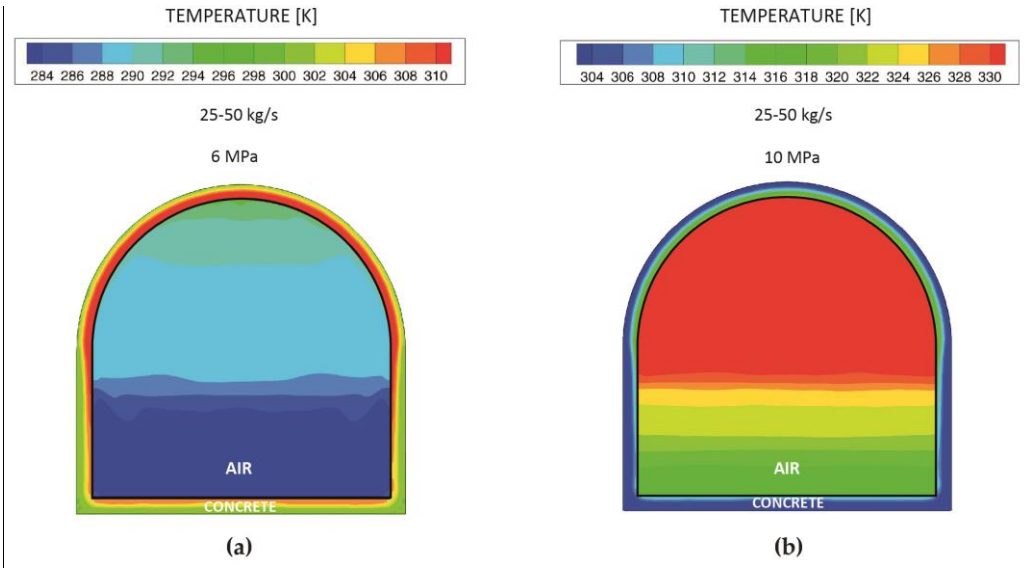

Fig. 7. Detail of the air and concrete lining temperature considering air mass flow rates of 25 kg s^{-1} in compression and 50 kg s^{-1} in expansion. (a) Air pressure of 6 MPa; (b) Air pressure of 10 MPa.

Fig. 8 depicts the distribution of the surface heat transfer on the surface between the compressed air and concrete lining at an air pressure of 6 MPa. The surface heat flux on the reservoir walls is shown in Fig. 9 at a pressure of 10 MPa, after air charging. At an air pressure of 6 MPa, the concrete lining temperature is higher than the air temperature over the entire surface and the heat flux is negative when an air mass flow rate of 25-50 kg s^{-1} is considered. However, due to the air temperature distribution within the reservoir, with a high air temperature on the roof, the direction of the heat flux varies depending on the area. As indicated in Fig. 8b, the concrete lining transfers thermal energy to the compressed air at the bottom of the reservoir. Fig. 10 shows the distribution of the heat transfer coefficient on the reservoir wall at a pressure of 10 MPa. An increase of the heat transfer coefficient is observed when the air mass flow rate increase up to 100 kg s^{-1}.

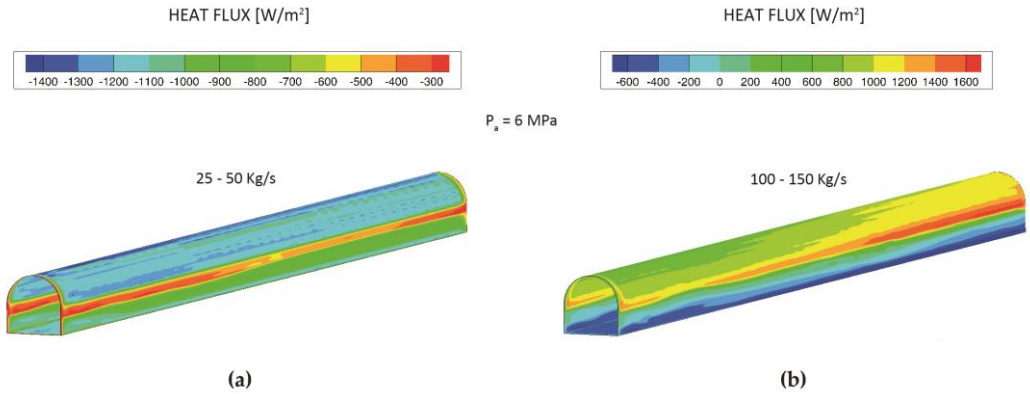

Fig. 8. Detail of the surface heat flux (Q_1) on the surface between compressed air and concrete lining at 6 MPa. (a) Air mass flow rates of 25-50 kg s^{-1}; (b) Air mass flow rates of 100-150 kg s^{-1}.

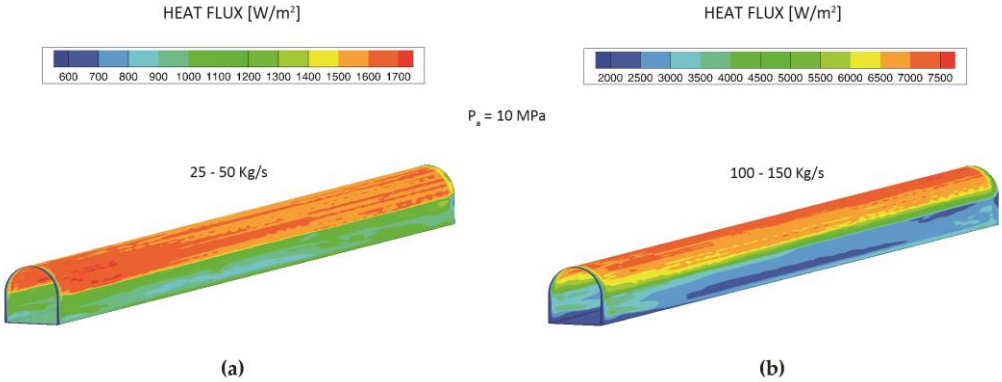

Fig. 9. Detail of the heat flux (Q_1) on the surface between compressed air and concrete lining at 10 MPa. (a) Air mass flow rates of 25-50 kg s^{-1}; (b) Air mass flow rates of 100-150 kg s^{-1}.

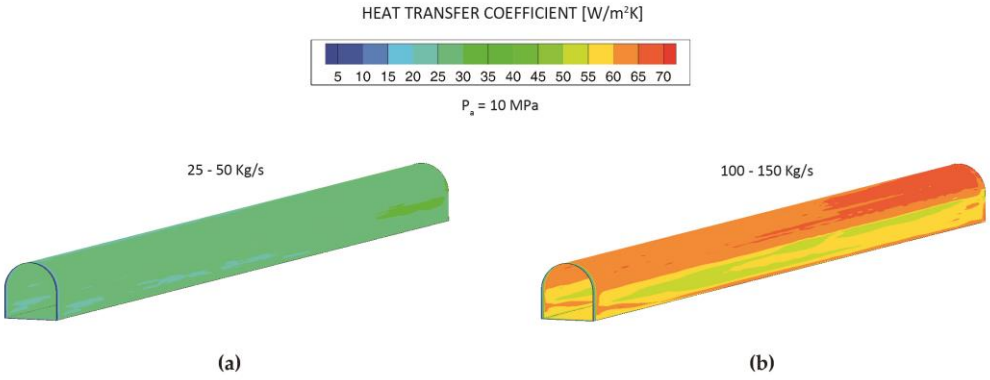

Fig. 10. Heat transfer coefficient on the surface between compressed air and concrete lining at 10 MPa. (a) Air mass flow rates of 25-50 kg s^{-1}; (b) Air mass flow rates of 100-150 kg s^{-1}.

3.2 Model validation

As indicated in section 2.2, the thermodynamic performance of the underground reservoir in A-CAES systems can also be simulated using analytical models. In order to validate the CFD modelling, a comparative analysis between numerical and analytical results is shown in Fig. 11. Air pressure and temperature are analyzed for the first operating cycle considering air mass flow rates of 25-50 kg s^{-1} and 100-150 kg s^{-1}.

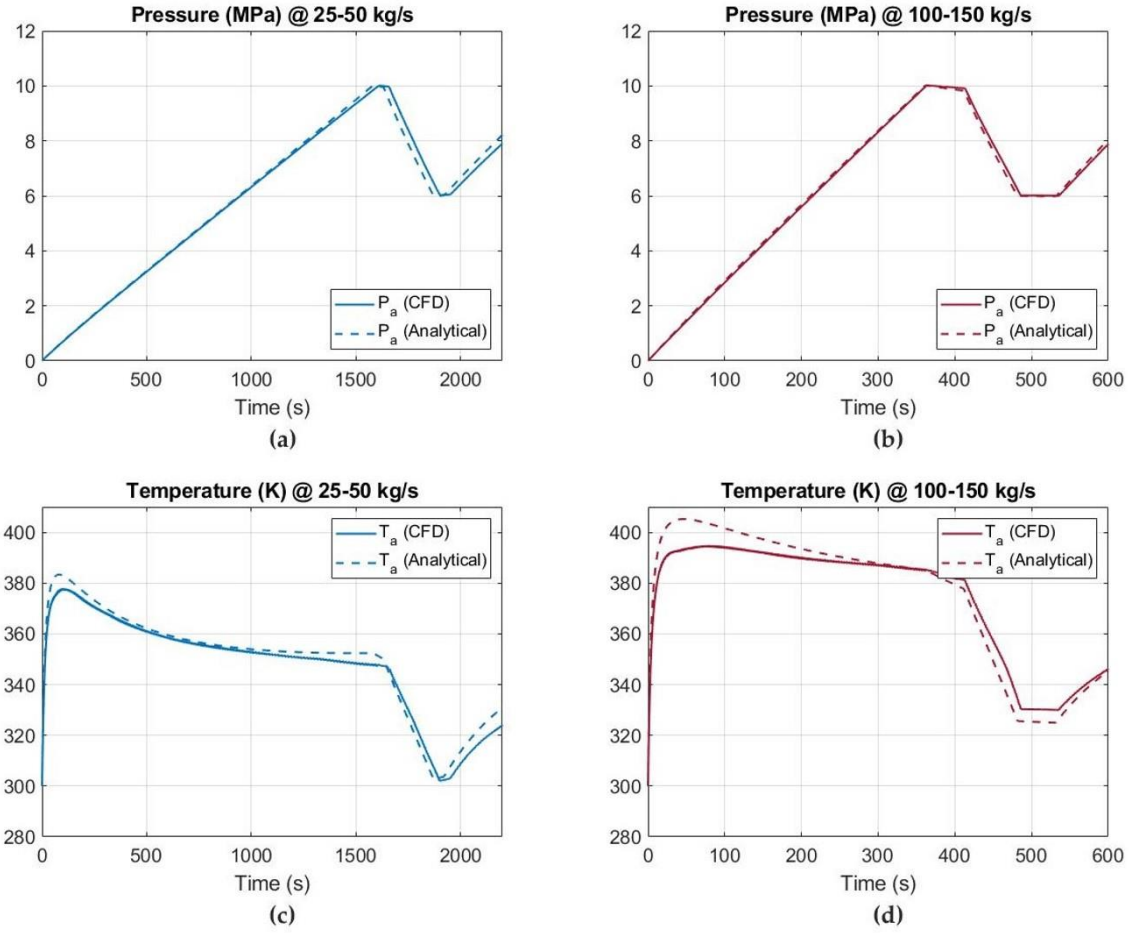

Fig. 11. Model validation. Comparative analysis for the first operation cycle between analytical and numerical results considering different operating conditions. (a) Air pressure @ 25-50 kg s^{-1}; (b) Air pressure @ 100-150 kg s^{-1}; (c) Air temperature @ 25-50 kg s^{-1}; (d) Air temperature @ 100-150 kg s^{-1}.

Finally, to validate the analytical model, the results obtained have been compared with other experimental and numerical research works. Fig. 12 depicts a comparative analysis with an experimental work conducted by Jiang et al. [17]. Air temperature and pressure have been analyzed during the first operation cycle. In addition, the results of the analytical model were also compared with a numerical modelling performed by Zhou et al. [13], as shown in Fig. 13. Air and wall temperatures and air pressure have been compared in the first cycle. In general, good agreements have been observed between the analytical model that has been developed and other research works existing in the literature.

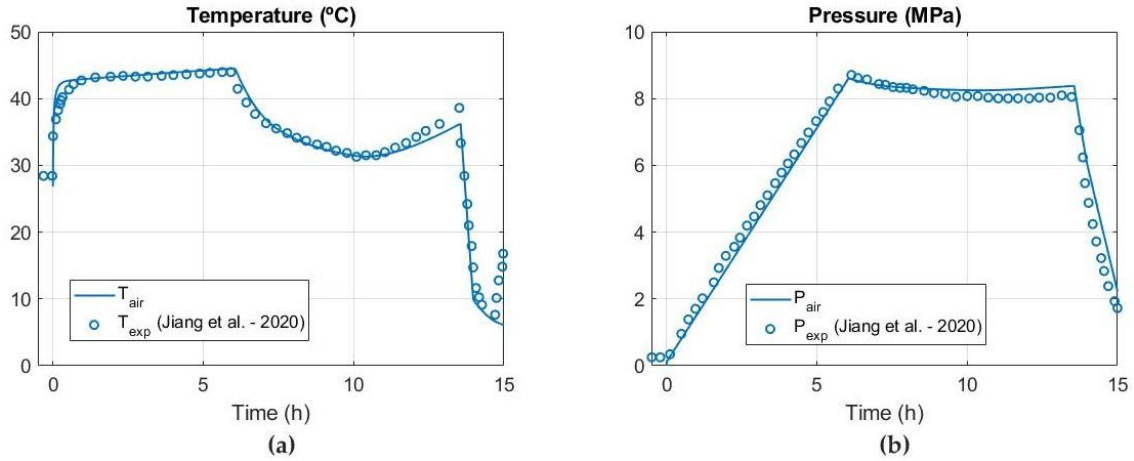

Fig. 12. Comparative analysis during the first cycle with an experimental research work conducted by Jiang et al. [17]. (a) Air temperature; (b) Air pressure.

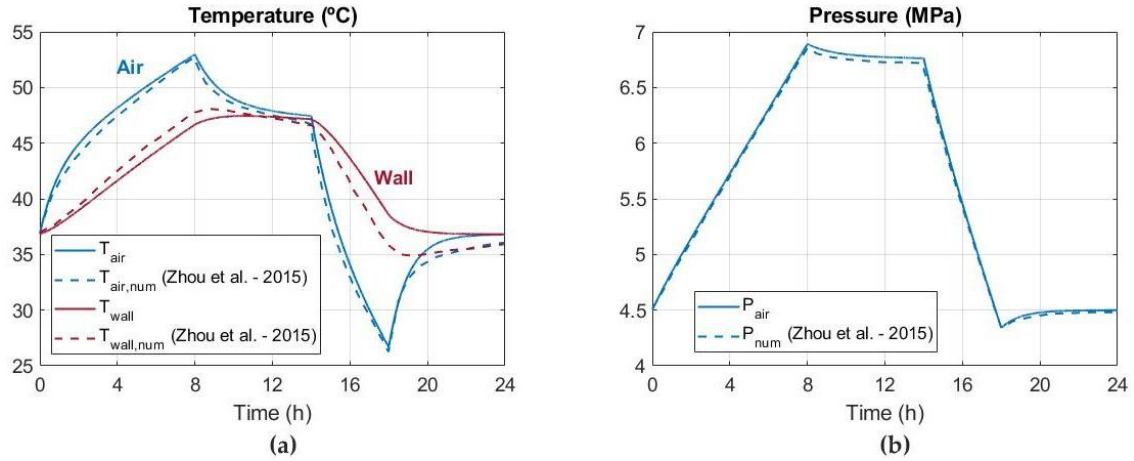

Fig. 13. Comparative analysis during the first cycle with a numerical model conducted by Zhou et al. [13]. (a) Air and wall temperature; (b) Air pressure.

3.3 Preliminary energy balance and global efficiency

The preliminary energy balance has been analyzed considering a constant reservoir capacity of 400 m^3 with operating pressures in the underground reservoir from 6 to 10 MPa. The energy consumption and production and the round-trip energy efficiency was estimated for different air mass flow rates in the compression and expansion processes. Therefore, a comparative analysis between different CAES models was carried out. The thermodynamic states of the LPC and HPC are shown in Table 4. In order to individually analyze the effect of the thermodynamic response of the reservoir on the global efficiency, compressors and turbines operate at a fixed point in nominal operating conditions. Ambient pressure and temperature are considered at the inlet of LPC (0.1 MPa, 293 K). Compression ratios of 13.82 and 7.14 have been applied in LPC and HPC, respectively. The air outlet temperature of the HPC reaches 896.20 K and is recovered by the TES system up to 310 K. Therefore, the air inlet temperature of the underground reservoir is 310 K.

Table 4
Thermodynamic states for the LPC and HPC.

Compression	LPC	HPC
Compressor inlet pressure (MPa)	0.1	1.40
Compressor outlet pressure (MPa)	1.4	10
Compression ratio	13.82	7.14
Compressor inlet temperature (K)	293.00	475.00
Compressor outlet temperature^{IS} (K)	620.44	833.02
Compressor outlet temperature (K)	676.42	896.20
Specific enthalpy 1 (KJ/kg)	293.55	478.80
Specific enthalpy 2 (KJ/kg)	689.00	933.98

The thermodynamic states of the HPT and LPT are shown in Table 5. Expansion ratios of 4 and 14.80 have been used in HPT and LPT, respectively. The HPT inlet temperature reaches 896.20 K while the LPT inlet temperature decreases down to 647.07 K.

Table 5
Thermodynamic states for the HPT and LPT.

Expansion	HPT	LPT
Turbine inlet pressure (MPa)	6.00	1.5
Turbine outlet pressure (MPa)	1.5	0.1
Expansion ratio	4.00	14.80
Turbine inlet temperature (K)	896.20	647.07
Turbine outlet temperature^{IS} (K)	603.10	299.61
Turbine outlet temperature (K)	647.07	349.99
Specific enthalpy 1 (KJ/kg)	932.21	657.78
Specific enthalpy 2 (KJ/kg)	657.78	351.01

The input power of the LPC and HPC is shown in Table 6. The input power of the compression process is 21.27 MW considering an air mass flow rate of 25 kg s^{-1} and 85.06 MW when an air mass flow rate of 100 kg s^{-1} is employed. Similarly, the output power of the HPT and LPT is shown in Table 7. The output power of the expansion train is 29.06 and 87.18 MW considering air mass flow rates of 50 and 150 kg s^{-1}, respectively.

Table 6
Input power of the LPC and HPC.

Air mass (kg/s)	LPC (MW)	HPC (MW)	Total (MW)
25	9.89	11.38	21.27
100	39.54	45.52	85.06

Table 7
Output power of the LPT and HPT.

Air mass (kg/s)	HPT (MW)	LPT (MW)	Total (MW)
50	13.72	15.34	29.06
150	41.16	46.01	87.18

The energy consumption is shown in Table 8 considering air mass flow rates of 25 and 100 kg s^{-1}. The energy consumption is reduced from 3.20 to 3.16 MWh $cycle^{-1}$ when the air mass flow rate increases from 25 to 100 kg s^{-1}. When the air mass flow rate increases, the air temperature is higher and therefore, the compression process from 6 to 10 MPa is faster. The power generation in the expansion train is shown in Table 9 for air mass flow rates of 50 and 150 kg s^{-1}. The power generation increases from 2.17 to 2.27

MWh cycle^{-1} when the air mass flow rate decreases from 150 to 50 kg s^{-1}. The total amount of air inside the reservoir at a pressure of 10 MPa increases from 41.96 to 43.80 t when the air mass flow rate in compression and expansion decrease down to 25-50 kg s^{-1}.

Table 8
Analysis of the energy consumption considering air mass flow rates of 25 and 100 kg s^{-1}.

Energy consumption	25 kg s^{-1}	100 kg s^{-1}
Storage capacity (m^3)	400	400
Minimum pressure (MPa)	6	6
Maximum pressure (MPa)	10	10
Total amount of air (t)	43.80	41.96
Input power (MW)	21.27	85.06
Charging time (h)	0.151	0.037
Energy consumption (MWh cycle^{-1})	3.20	3.16

Table 9
Analysis of the power generation considering air mass flow rates of 50 and 150 kg s^{-1}.

Energy production	50 kg s^{-1}	150 kg s^{-1}
Storage capacity (m^3)	400	400
Minimum pressure (MPa)	6	6
Maximum pressure (MPa)	10	10
Total amount of air (t)	43.80	41.96
Output power (MW)	29.06	87.18
Discharging time (h)	0.078	0.025
Energy production (MWh cycle^{-1})	2.27	2.17

The energy balance considering and the global efficiency for daily production cycles are shown in Table 10. A round-trip energy efficiency of 0.71 is achieved for air mass flow rates of 25 kg s^{-1} (charge) and 50 kg s^{-1} (discharge) while it is reduced down to 0.68 for air mass flow rates of 100 kg s^{-1} (charge) and 150 kg s^{-1} (discharge). The results obtained show that the round-trip efficiency improves when the air temperature fluctuations within the underground reservoir are reduced. The air temperature reduction can be produced increasing the thermal conductivity of the materials around the compressed air (sealing layer, concrete lining and rock mass) or decreasing the air mass flow rates in the compression and expansion processes. A high thermal conductivity concrete could increase the storage capacity and therefore the amount of stored energy. Moreover, lower injected air temperatures at the outlet of the TES system (inlet of the underground reservoir) also increase the round-trip efficiency of the A-CAES system.

Table 10
Energy balance and global efficiency.

Global efficiency	25-50 kg s^{-1}	100-150 kg s^{-1}
Energy consumption (MWh year^{-1})	1,089.38	1,076.09
Energy production (MWh year^{-1})	772.06	736.56
Round-trip efficiency	0.71	0.68

4 Conclusions

U-shaped mining drifts in abandoned mines are proposed as underground reservoirs for A-CAES plants. Three-dimensional CFD numerical models have been performed to investigate the thermodynamic response of the reservoir during the operation time. In addition, to validate the CFD results, a one-dimensional analytical model has also been developed. Air temperature and pressure variations within the reservoir and heat transfer across the reservoir walls have been analyzed for ten compression and expansion cycles at different operating conditions.

The results obtained indicate that the air temperature within the underground reservoir increases when the air mass flow rate increases in the compression process from 25 to 100 kg s^{-1}. The air temperature reaches 322 and 335 K after air charging for 25 and 100 kg s^{-1}, respectively. The concrete lining temperature reaches 340 K on the roof of the lined mining drift in the compression process considering an air mass flow rate of 100 kg s^{-1}. However, no temperature variations were observed in the rock mass during the operation of the A-CAES systems.

The storage capacity increases when the air mass flow rate and the air temperature within the underground reservoir decrease. In addition, the power generation and the round-trip energy efficiency also increase when the variations in air temperature are reduced. A 4.60% increase in power generation was observed in the expansion process when the air mass flow rate is reduced from 150 to 50 kg s^{-1}.

The round-trip efficiency reaches 0.71 for a CAES scheme with air mass flow rates of 25 and 50 kg s^{-1} in compression and expansion, respectively. The global efficiency is reduced down to 0.68 when the air mass flow rates increase up to 100-150 kg s^{-1}. Finally, we can conclude that the global efficiency and the power generation of A-CAES systems can be increased by using lower air mass flow rates and injected air temperatures and higher thermal conductivity concrete lining.

References

[1] X Luo, J Wang, M Dooner, J Clarke. Overview of current development in electrical energy storage technologies and the application potential in power system operation. Applied Energy 137 (2015) 511-536.

[2] E R Barbour, D L Pottie, Eames P. Why is adiabatic compressed air energy storage yet to become a viable energy storage option?, iScience 24(5) 2021 102440.

[3] F Winde, F Kaiser, E Erasmus, Exploring the use of deep level gold mines in South Africa for underground pumped hydroelectric energy storage schemes. Renew Sustain Energy Rev 78 (2016) 668–682.

[4] R Madlener, JM Specht. An exploratory economic analysis of underground pumped-storage hydro power plants in abandoned coal mines. FCN Working Paper No. 2/2013.

[5] J. Menendez, J Loredo, J.M. Fernandez-Oro, M Galdo. Energy storage in underground coal mines in NW Spain: Assessment of an underground lower water reservoir and preliminary energy balance. Renew. Energy 134 (2019) 1381-1391.

[6] J Menendez, A. Ordoñez, R. Alvarez, J. Loredo, Energy from closed mines: underground energy storage and geothermal applications, Renew. Sustain. Energy Rev. 108 (2019) 498-512.

[7] Pujades E, Orban P, Bodeux S, Archambeau P, Erpicum S, Dassargues A. Underground pumped storage hydropower plants using open pit mines: how do groundwater exchanges influence the efficiency? Appl Energy 190 (2017) 190 135–46.

[8] J Menéndez, JM Fernandez-Oro, M Galdo, J Loredo. Efficiency analysis of underground pumped storage hydropower plants. J. Energy Storage 28 (2020) 101234

[9] J Menendez, J.M. Fernandez-Oro, M. Galdo, J. Loredo, Pumped-storage hydropower plants with underground reservoir: influence of air pressure on the efficiency of the Francis turbine and energy production, Renew. Energy. 143 (2019) 1427-1438.

[10] M. Nakhamkin, L. Andersson, E. Swensen, J. Howard, R. Meyer, R. Schainker, et al., AEC 110 MW CAES plant: status of project, J. Eng. Gas Turbines Power 114 (1992) 695–700.

[11] M. Lutyński, An overview of potential benefits and limitations of compressed air energy storage in abandoned coal mines, IOP Conf. Ser. Mater. Sci. Eng. 268 (2017) 012006.

[12] S. Succar, R.H. Williams, Compressed air energy storage: theory, resources, and applications for wind power, Princeton Environ. Inst. Rep. (2008) 8.

[13] S Zhou, C Xia, H Zhao, S Mei, Y Zhou. Numerical simulation for the coupled thermo-mechanical performance of a lined rock cavern for underground compressed air energy storage. Journal of Geophysics and Engineering 14(6) (2017) 1382–1398

[14] S Zhou, C Xia, S Du, P Zhang, Y Zhou. An Analytical Solution for Mechanical Responses Induced by Temperature and Air Pressure in a Lined Rock Cavern for Underground Compressed Air Energy Storage. Rock Mech Rock Eng 48 (2015) 749–770.

[15] L Geissbühler, V Becattini, G Zanganeh, S Zavattoni, M Barbato, A Haselbacher, A Steinfeld. Pilot-scale demonstration of advanced adiabatic compressed air energy storage, Part 1: Plant description and tests with sensible thermal-energy storage. J. Energy Storage 17 (2018) 129–139.

[16] V Becattini, L Geissbühler, G Zanganeh, A Haselbacher, A Steinfeld. Pilot-scale demonstration of advanced adiabatic compressed air energy storage, Part 2: Tests with combined sensible/latent thermal-energy storage. J. Energy Storage 17 (2018) 140–152.

[17] Z Jiang, P Li, D Tang, H Zhao, Y Li. Experimental and Numerical Investigations of Small-Scale Lined Rock Cavern at Shallow Depth for Compressed Air Energy Storage. Rock Mech Rock Eng 53 (2020) 2671–2683.
[18] S Wang, X Zhang, L Yang, Y Zhou, J Wang Experimental study of compressed air energy storage system with thermal energy storage. Energy 103 (2016) 182-191.
[19] F Schmidt, J Menéndez, H Konietzky, P Pascual-Muñoz, J Castro, J Loredo, A Bernardo-Sánchez. Converting closed mines into giant batteries: effects of cyclic loading on the geomechanical performance of underground compressed air energy storage systems. Journal of Energy Storage 32 (2020) 101882.
[20] L Alvarez, J Menendez, A Bernardo-Sanchez, M Galdo, J Loredo, JM Fernandez-Oro. Thermodynamic analysis of compressed air energy storage (CAES) reservoirs in abandoned mines using different sealing layers. App Sci 11, (2021) 2573.
[21] R Kushnir, A Dayan, A Ullmann. Temperature and pressure variations within compressed air energy storage caverns Int. J. Heat Mass Transfer 55 (2012) 5616–30.
[22] S Sarmast, R. A. Fraser, M. B. Dusseault. Performance and cyclic heat behavior of a partially adiabatic Cased-Wellbore Compressed Air Energy Storage system. J Energy Storage 44 (2021) 103279.
[23] K Khaledi, E Mahmoudi, M Datcheva, T Schanz. Analysis of compressed air storage caverns in rock salt considering thermomechanical cyclic loading. Environmental Earth Sciences 75 (2016) 1149.
[24] J Rutqvist, HM Kim, DW Ryu, JH Synn, WK Song. Modeling of coupled thermodynamic and geomechanical performance of underground compressed air energy storage in lined rock caverns. Int. J. Rock Mech. Min. Sci 52 (2012) 71–81.
[25] S Mohanto, K Singh, T Chakraborty, D Basu. Cyclic thermo-mechanical analysis of wellbore in underground compressed air energy storage cavern. Geotech Geol Engi 32 (2014) 601-616.
[26] H Kim, J Rutqvist, J Jeong, B Choi, D Ryu, W Song. Characterizing excavation damaged zone and stability of pressurized lined rock caverns for underground compressed air energy storage. Rock Mech Rock Eng 46 (2013) 1113–1124.
[27] Kim H, Rutqvist J, Kim H, Park D, Ryu D, Park E (2016) Failure monitoring and leakage detection for underground storage of compressed air energy in lined rock caverns. Rock Mech Rock Eng 49 (2016) 573–584
[28] JW Chen, WD Jiang, CH Yang, XY Yin, SW Fu and KJ Yu. Study on engineering thermal analysis of gas storage in salt formation during gas injection and production Chin. J. Rock Mech. Eng. 26 (2007) 2887–94.
[29] V Tola, V Meloni, F Spadaccini, G Cau. Performance assessment of Adiabatic Compressed Air Energy Storage (A-CAES) power plants integrated with packed-bed thermocline storage systems. Energy Convers Manag 151 (2017) 343–56
[30] A Sciacovelli, Y Li, H Chen, Y Wu, J Wang, S Garvey, Ding Y. Dynamic simulation of Adiabatic Compressed Air Energy Storage (A-CAES) plant with integrated thermal storage – Link between components performance and plant performance. Appl Energy 185 (2017) 16–28.
[31] JL Liu, JH Wang. A comparative research of two adiabatic compressed air energy storage systems. Energy Convers Manage 108 (2016) 566–78.
[32] E Barbour, D Mignard, Y Ding, Y Li. Adiabatic compressed air energy storage with packed bed thermal energy storage. Appl. Energy 155 (2015) 804–815.
[33] Y Li, S Miao, X Luo, B Yin, J Han, J Wang. Dynamic modelling and techno-economic analysis of adiabatic compressed air energy storage for emergency back-up power in supporting microgrid. Applied Energy 261 (2020) 114448.
[34] M Dooner, J Wang. Potential Exergy Storage Capacity of Salt Caverns in the Cheshire Basin Using Adiabatic Compressed Air Energy Storage. Entrophy 21 (2019) 1065.
[35] W He, X Luo, D Evans, J Busby, S Garvey, D Parkes, J Wang. Exergy storage of compressed air in cavern and cavern volume estimation of the large-scale compressed air energy storage system. Applied Energy 208 (2017) 745-757.
[36] M King, A Jain, R Bhakar, J Mathur, J Wang. Overview of current compressed air energy storage projects and analysis of the potential underground storage capacity in India and the UK. Renewable and Sustainable Energy Reviews 139 (2021) 110705.
[37] D Evans, D Parkes, M Dooner, P Williamson, J Williams, J Busby, W He, J Wang, S Garvey. Salt cavern exergy storage capacity potential of UK massively bedded halites, using compressed air energy storage (CAES). Applied Sciences 11 (2021) 472.
[38] Y Xu, S Zhou, C Xia, H Zhao, X Xue. Three-dimensional thermo-mechanical analysis of abandoned mine drifts for underground compressed air energy storage: A comparative study of two construction and plugging schemes. J Energy Storage 39 (2021) 102696.
[39] S B Mousavi, M Adib, M. Soltani, A R Razmi, J Nathwani. Transient thermodynamic modeling and economic analysis of an adiabatic compressed air energy storage (A-CAES) based on cascade packed bed thermal energy storage with encapsulated phase change materials. Energy Convers Manag 243 (2021) 114379.

[40] M Zeynalian, A H Hajialirezaei, A R Razmi, M Torabi. Carbon Dioxide Capture from Compressed Air Energy Storage System. Applied Thermal Engineering 178 (2020) 115593.
[41] A R Razmi, M Janbaz. Exergoeconomic assessment with reliability consideration of a green cogeneration system based on compressed air energy storage (CAES) Energy Convers Manag 204 (2017) 112320.
[42] S M Alirahmi, A R Razmi, Ahmad Arabkoohsar. Comprehensive assessment and multi-objective optimization of a green concept based on a combination of hydrogen and compressed air energy storage (CAES) systems. Renewable and Sustainable Energy Reviews 142 (2021) 110850.
[43] A R Razmi, M Soltani, A Ardehali, K Gharali, M.B. Dusseault, J Nathwani. Design, thermodynamic, and wind assessments of a compressed air energy storage (CAES) integrated with two adjacent wind farms: A case study at Abhar and Kahak sites, Iran. Energy 221 (2021) 119902.
[44] A R Razmi, H H Afshar, A Pourahmadiyan, M. Torabi. Investigation of a combined heat and power (CHP) system based on biomass and compressed air energy storage (CAES). Sust Energy Techn and Assess 46 (2021) 101253.
[45] R Kushnir, A Ullmann, A Dayan. Compressed air flow within aquifer reservoirs of CAES plants. Transp Porous Med 81 (2010) 219–240.
[46] H Zhou, H Xie, J Zuo. Research progress of rock mechanical behavior under deep high ground stress Adv. Mech. 1 (2005) 91-99
[47] S Wang S, L Jian, Z Shu, Chen S, Chen L. A high thermal conductivity cement for geothermal exploitation application. Natural Resources Research 29 (2020) 3675–3687.
[48] Q Li, L Chen, H Ma, CH Huang. Enhanced Heat Transfer Characteristics of Graphite Concrete and Its Application in Energy Piles", Advances in Materials Science and Engineering, 2018 (2018) 8142392.
[49] W Guo, Z Zuo, J Sun, H Hou, Q Liang, H Chen. Experimental investigation on off-design performance and adjustment strategies of the centrifugal compressor in compressed air energy storage system. J Energy Storage 38 (2021) 102515.